Quantitative magnetic resonance imaging evaluation of hepatic fat content with iron deposition: will it be disturbed?

**Qian Wang[1,2], Feng Ye[2], Peiqing Ma[3],
Feng Chen[4], Yiqun Che[2], Xinming Zhao[2] and
Li Yang[1]** (ID)

Abstract

Objective: To explore noninvasive assessment of liver fat content with iron deposition using magnetic resonance (MR) quantitative technology.

Methods: A water–fat phantom with iron deposition containing 63 vials with predetermined fat percentages and iron concentrations was constructed. Thirty-three patients underwent fat quantitative MR examinations. The fat fraction (FF) was determined by three Dixon techniques. Pathological evaluation findings and the steatosis area rate (SAR) were used as the gold standards.

Results: FF_{IOP} and $FF_{LAVA-Flex}$ significantly differed from FF_{TEST} for iron concentrations of 1 to 30 µg/mL and fat components of 10% to 80%. Using the three Dixon techniques, FF_{IOP} was 15.76% ± 6.98%, $FF_{LAVA-Flex}$ was 16.71% ± 6.77%, and $FF_{IDEAL\ IQ}$ was 13.18% ± 6.42% in patients without liver cirrhosis; these values in patients with liver cirrhosis were 20.35% ± 6.11%, 20.89% ± 8.49%, and 12.86% ± 4.00%, respectively. The SAR in patients without and with liver cirrhosis was 11.31% ± 5.89% and 9.84% ± 4.17%, respectively. There were significant positive correlations between $FF_{IDEAL\ IQ}$ and SAR with or without liver cirrhosis.

[1]Department of Radiology, Chinese PLA General Hospital, Medical School of Chinese PLA, Beijing, China
[2]Department of Imaging Diagnosis, National Cancer Center/National Clinical Research Center for Cancer/Cancer Hospital, Chinese Academy of Medical Sciences and Peking Union Medical College, Beijing, China
[3]Department of Pathology, National Cancer Center/National Clinical Research Center for Cancer/Cancer Hospital, Chinese Academy of Medical Sciences and Peking Union Medical College, Beijing, China

[4]Department of Pharmacy, National Cancer Center/National Clinical Research Center for Cancer/Cancer Hospital, Chinese Academy of Medical Sciences and Peking Union Medical College, Beijing, China

Corresponding author:
Li Yang, Department of Radiology, Chinese PLA General Hospital, Medical School of Chinese PLA, No. 28 Fuxing Road, Haidian District, Beijing 100853, China.
Email: yangli2017@yeah.net

Conclusion: Iron deposition must be considered when using quantitative MR techniques to evaluate the hepatic fat content. Compared with the IOP and LAVA-Flex techniques, the IDEAL IQ technique has more stability and accuracy in measurement of the hepatic fat content, free from iron deposition.

Introduction

Hepatic steatosis is caused by several chronic liver diseases and drug reactions; it is also the main change in the early stages of many diffusive liver diseases.[1] Hepatic steatosis may evolve into steatohepatitis, liver fibrosis, cirrhosis, and even hepatocellular carcinoma, which can ultimately lead to liver failure.[2] Fatty infiltration is an obvious indicator of steatosis and often occurs in the hepatocytes of patients affected by non-alcoholic fatty liver disease (NAFLD).[3,4] Steatohepatitis reflects drug-induced liver damage by anticancer drugs, anti-tuberculosis drugs, and nonsteroidal anti-inflammatory drugs.[5–9] Thus, accurate and quantitative assessment of the liver fat content is crucial when monitoring drug reactions, predicting postoperative risk, and assessing donor suitability before liver transplantation.[10]

The Dixon techniques based on magnetic resonance (MR) imaging have recently become widely used in fat content quantification.[11,12] Although many reports have described these fat–water separation applications,[13–16] the complexity of the liver microenvironment is often not considered. The most important consideration is that the sensitivity of the hepatic fat fraction (FF) may be affected by unknown substances in the liver microenvironment, such as iron deposition. Recent studies have shown that ferritin and hemosiderin can play prominent roles in the uniformity of the main magnetic field and that hydrogen proton T_2^* relaxation accelerates and interferes with detection of the fat signal. These conditions may bring about changes in local B_0 homogeneity, T1 and $T2^*$ relaxation times, and the fat spectrum amplitude and distribution.[16,17] The most recent studies have considered the simultaneous conditions of hepatic iron overload and hepatic fat accumulation and their synergistic interactions.[18] Iron overload caused by alcoholic fatty liver disease, NAFLD, drug reactions, hepatitis virus infection, and repeated blood transfusion can aggravate hepatic steatosis, which may evolve into cryptogenic cirrhosis and even hepatic carcinoma. Liver injury caused by fatty degeneration also results in the accumulation of ferritin and hemosiderin in the liver microenvironment.[19,20] These potential changes in the liver microenvironment force us to consider the effects of iron deposition when evaluating the fat content. International standards of iron overload have not been unified. Iron overload (serum ferritin concentration of $>1 \mu g/mL$) can markedly affect the homogeneity of the magnetic field as described in previous reports. This affects the in-phase

and out-of-phase times, leading to changes in the signal intensity (SI) in voxels as well as errors in water–fat separation based on the quantitative FF.[20]

In this study, three Dixon techniques, namely in-phase and out-of-phase (IOP) imaging, the liver imaging with volume acceleration-flexible (LAVA-Flex) sequence, and the iterative decomposition of water and fat with echo asymmetry and least-squares estimation quantification sequence (IDEAL IQ), were compared *in vitro* and *in vivo*. The purpose of this study was to explore whether these three methods can accurately quantify the hepatic fat content in the presence of iron deposition.

Materials and methods

Preparation of water–fat phantom with iron deposition

As described in previous reports, we prepared a water–fat phantom with iron deposition comprising 63 18-mL polyvinyl chloride vials of known fat volume percentages (9 vials in 10% increments from 0% to 80%) and iron concentrations (0, 1, 4, 8, 10, 20, and 30 µg/mL).[21,22] Vegetable oil was used because it has a proton nuclear magnetic resonance spectrum similar to that of the triglyceride protons in adipose tissue.[17] Appropriate vegetable oil ($\rho = 0.896$ g/cm^3) was dispensed by weight into vials to simulate fat stacking in hepatocyte cytoplasm. We used deionized water as a soluble medium for iron in this study. Lecithin, as a double surfactant with both hydrophilic and hydrophobic properties, was used at a 100-µg/mL concentration in the merged water and oil phases. Dextriferron is an important iron supplement formulation and can shorten T2* relaxation.[23] In the present study, water-soluble iron dextran (5 mg/mL; Pharmacosmos A/S, Holbaek, Denmark) was used to mimic iron overload and was diluted in deionized water at a 1:10 ratio. The iron dextran solution was then obtained in several aliquots (0, 10, 40, 80, 100, 200, and 300 µL) and titrated with the water–oil phantom. The solutions were homogeneous and mingled with iron concentrations of 0, 1, 4, 8, 10, 20, and 30 µg/mL, respectively, in each of the 9 groups, forming a total of 63 test tubes. A super-shear emulsifying machine (FM300; Fluko, Shanghai, China) was used to splinter the large water and oil particles into small ones to overcome their surface tension. A high-pressure homogenizer (APV-2000; Berlin, Germany) was used to blend the phantom samples and facilitate the formation of oil-in-water or water-in-oil products.

Phantom scanning

Phantom imaging acquisition was conducted on a 3.0T MR imaging scanner (Discovery MR 750; GE Healthcare, Chicago, IL, USA) using an 8-channel head coil. The water–oil phantom was fixed on the tray and placed in the center of the head coil. All examinations were performed in the supine position. The sequences included fast-spoiled gradient echo T1-weighted imaging with a two-point Dixon technique for the IOP, LAVA-Flex, and IDEAL IQ methods. The scan parameters for the three different fat quantification methods are shown in Table 1.

Phantom imaging analysis

Phantom imaging analysis was performed on the vendor-supplied workstation (Advantage Workstation 4.6; GE Healthcare). The FF was measured in regions of interest (ROIs) in the three-dimensional (3D) dual-echo sequences, and LAVA-Flex sequences were defined using the images of each tube for each acquisition. The images from the IP and OP images in the 3D dual-echo sequence and the water and fat phases in the LAVA-Flex sequence were spatially registered. The central area of

Table 1. Magnetic resonance imaging parameters of fat quantitation *in vitro*.

Sequence	TR (ms)	TE (ms)	Flip angle	Matrix	NEX	Bandwidth (kHz)	FOV (cm^2)	Slice/space (mm)	Scan time (s)
IOP	120	1.1–2.3	15°, 70°	192 × 224	0.5	143	16 × 16	3/0	16
LAVA-Flex	4	2.4	15°	192 × 224	1	167	16 × 16	3/0	11
IDEAL IQ	10	1.2	3°	192 × 224	0.5	125	16 × 16	3/0	20

Note. IOP: in-phase and out-of-phase; LAVA-Flex: liver imaging with volume acceleration-flexible; IDEAL IQ: iterative decomposition of water and fat with echo asymmetry and least square estimation-quantitative fat imaging; TR: time of recovery; TE: time of echo; NEX: number of excitations; FOV: field of view.

the cross section of the test tube was selected as the ROI so that it was as far as possible from the edge of the tube to avoid magnetic susceptibility artifacts. The ROI area was 1.5 cm^2 given an effective inner diameter of 1.8 cm, and the ROIs were copied to different images to ensure consistency. For the IOP images, the FF value was calculated using Formula (1), where the SI for IP and OP (SI_{IP} and SI_{OP}) are the SI levels measured on the IP and OP images, respectively. For the LAVA-Flex images, the FF value was calculated using Formula (2), where SI_{water} and SI_{fat} are the SIs measured on the pure water and pure fat images, respectively. For the IDEAL IQ images, the $FF_{IDEAL\ IQ}$ and R2* were measured on FF mapping and R2* mapping according to the Formula (3) algorithm.

$$FF_{IOP} = 100 \times [(SI_{IP} - SI_{OP})/2 \times SI_{IP}] \quad (1)$$

$$FF_{water-fat} = 100 \times [SI_{fat}/(SI_{fat} + SI_{water})] \quad (2)$$

$$FF_{IdealIQ} = \frac{SI_{IP}*e^{-TE/T2*}SI_{OP}}{2*SI_{IP}*e^{(-TE/T2*)}} \quad (3)$$

Patient enrollment and MR imaging

This study was approved by the Cancer Hospital ethics committee. The clinical trial was registered at the Chinese Clinical Trial Registry (No. ChiCTR1800015242). In total, 32 adult patients who underwent hepatic excision from October 2016 to April 2018 were recruited in this study. Written informed consent was obtained from all patients. Six patients were excluded due to claustrophobia (n = 1), metal artifact (n = 1), and respiratory motion artifacts (n = 4). The final study population comprised 26 patients (18 men, 8 women; age range, 37–64 years). The patients were highly suspected to have hepatocellular carcinoma (n = 11) or liver metastases (n = 15). Of the 26 patients, 17 had no biochemical abnormalities and 9 had a history of cirrhosis. The clinical information of all patients was acquired. All patients underwent MR examinations on a 3.0T MR scanner (Discovery MR 750; GE Healthcare) using 8-channel phased-array coils. All examinations were performed within 1 week before liver resection. The three Dixon sequence parameters used are shown in Table 2.

Patient imaging analysis

The FF_{IOP}, $FF_{LAVA-Flex}$, and $FF_{IDEAL\ IQ}$ were calculated in the clinical study. The ROIs were manually chosen with avoidance of obvious lesions, vessels, and artifacts within the same segment. All measurements were made by an experienced radiologist who had 6 years of experience and was blinded to the pathological results.

Table 2. Magnetic resonance imaging parameters for clinical study.

Sequence	TR (ms)	TE (ms)	Flip angle	Matrix	NEX	Bandwidth (kHz)	FOV (cm × cm)	Slice/space (mm)	Scan time (s)
IOP	120	1.1–2.3	15°,70°	192 × 224	0.5	143	20 × 24	3/0.6	16
LAVA-Flex	4	2.4	15°	192 × 224	1	167	20 × 24	3/0.6	15
IDEAL IQ	10	1.2	3°	192 × 224	0.5	125	20 × 24	3/0.6	24

Note. IOP: in-phase and out-of-phase; LAVA-Flex: liver imaging with volume acceleration-flexible; IDEAL IQ: iterative decomposition of water and fat with echo asymmetry and least square estimation-quantitative fat imaging; TR: time of recovery; TE: time of echo; NEX: number of excitations; FOV: field of view.

Pathological assessments

The pathological results of the liver resection were used as the gold standard for liver steatosis and fibrosis. All histopathological assessments were performed using a ×40 microscope by two pathologists with more than 5 years of diagnostic experience. Liver steatosis was scored based on the proportion of hepatocytes containing lipid droplets. ROIs of 1 cm^2 were placed outside the liver tumor tissue. The steatosis area rate (SAR) was calculated using Formula (4).

$$SAR = \frac{Area_{steatosis}}{Area_{net}} \times 100\% \qquad (4)$$

Statistical analysis

Paired t tests were performed to determine whether statistical significance existed between the FF measurements and the fat content. One-sided analysis of variance was used to determine whether statistically significant differences in the measured FF values existed between measurements obtained using IOP, LAVA-Flex, and IDEAL IQ. Linear regression was performed between the known FFs and the measured FFs obtained from the different imaging methods. Spearman's correlation coefficient was used to compare the consistency among the results obtained from the

three different techniques and the SAR in the groups with or without cirrhosis.

Results

Phantom equivalent evaluation

Figure 1 shows the vials with 10% fat and increasing iron concentrations (left to right) from 0 to 30 μg/mL. Oil-in-water models were visible as round structures, and iron dextrin was uniformly dissolved in water. Increasing iron concentrations darkened the color of the water. The solutions with setp-up iron concentrations were displayed on a particle sizing distribution graph (Particle Sizing Systems, Santa Barbara, CA, USA). Based on the intensity-weighted Gaussian distribution analysis for water and 10% oil phantom, the mean diameter was estimated as 202.5 nm and standard deviation as 70.1 nm; the 75% oil-in-water particles of the distribution were estimated to be <240.7 nm. The particle sizing followed a Gaussian distribution, indicating stable and successful emulsification as a micro-emulsion solution.

Phantom homogeneity evaluation

Three points were selected to measure the SI from top to bottom. The ROI was placed by one investigator with more than 5 years of MR diagnostic experience, and the area of the ROI was 1.5 cm^2 (less than the area of the tube wall). The homogeneity of
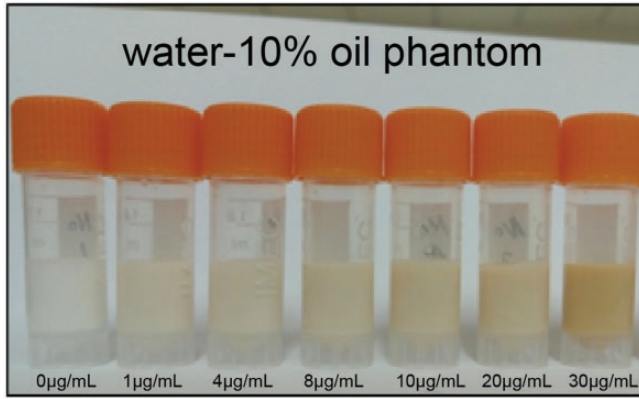
Figure 1. Water–10% oil phantom with water-soluble iron dextran concentrations from 0 to 30 μg/mL (left to right). The phantom was a homogeneous oil-in-water model.
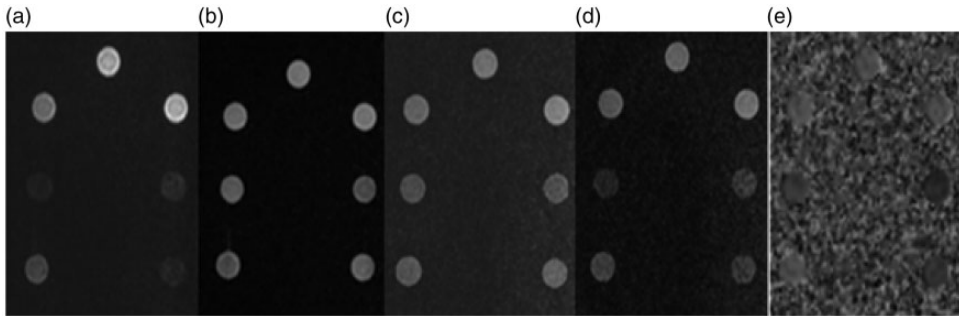

Figure 2. Water–10% oil phantoms were scanned by IOP, LAVA-Flex, and IDEAL IQ sequences and analyzed. (a, b) IOP imaging. (c, d) LAVA-Flex imaging. (e) Fat mapping of IDEAL IQ imaging.

the model was evaluated using the average value of the difference among the three slices. The SI deviations at the adjacent slices were within 10%.

Phantom analysis

The phantom content comprised water, vegetable oil, and iron emulsified by lecithin. The water–oil phantom with iron deposition was scanned via IOP, LAVA-Flex, and IDEAL IQ sequences, and the SI values are shown in Figure 2. When the oil content was <50%, the oil-in-water phase was steady. However, when the oil content exceeded the water content, the balance of oil and water was disturbed, and phase inversion occurred. When the oil content was >50%, the water-in-oil phase was relatively stable. Figure 3 shows the measured FF against the known FF (FF_{TEST}) for all iron concentrations produced in the IOP condition. The paired t test results regarding changes in the measured FF at various iron concentrations and the distribution of the 95% confidence interval (CI) are summarized in Table 3. The results regarding fitting of the linear regression are summarized in Table 4. As shown in Figure 3, the higher the iron concentration,
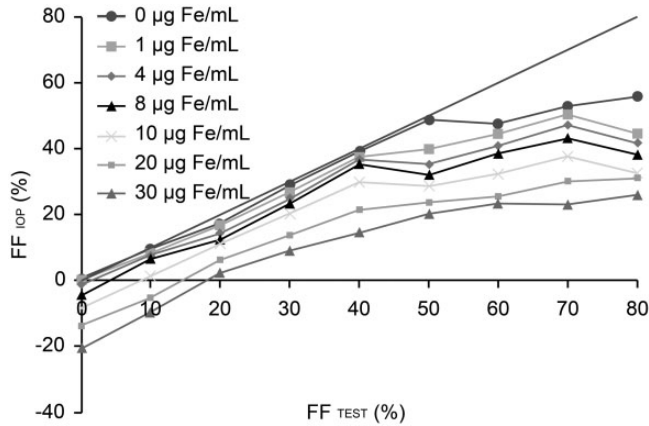
Figure 3. Measured fat fraction against known fat fraction (FF$_{TEST}$). The FF$_{TEST}$ and FF$_{IOP}$ technique measured the water–oil phantom with iron deposition at concentrations of 0 to 30 µg/mL.

Table 3. Comparison of measured FF$_{IOP}$ (%) and FF$_{TEST}$ (%) by paired t test.

Iron concentration (µg/mL)	Difference in pairs				t	p
	Mean	SD	SE	95% CI		
0	8.67	8.89	3.96	0.36–13.5	2.35*	0.045
1	9.46	11.86	3.95	0.3–18.5	2.39*	0.044
4	11.52	12.54	4.18	1.8–19.4	2.75*	0.025
8	13.68	13.37	4.45	3.4–21.6	3.07*	0.015
10	18.05	14.21	4.73	7.1–28.9	3.81**	0.005
20	23.63	13.65	4.55	13.1–34.1	5.19**	0.001
30	30.22	12.95	4.31	20.2–40.1	7.00***	0.000

Note. FF$_{IOP}$: fat fraction of IP-OP sequence; FF$_{TEST}$: known fat fraction; SD: standard deviation; SE: standard error; CI: confidence interval. *$p < 0.05$; **$p < 0.01$; ***$p < 0.001$.

Table 4. Linear regression between FF$_{IOP}$ (%) and FF$_{TEST}$ (%).

	Test rating	0 µg Fe/mL	1 µg Fe/mL	4 µg Fe/mL	8 µg Fe/mL	10 µg Fe/mL	20 µg Fe/mL	30 µg Fe/mL
Intercept	F	123.41	52.94	46.44	36.12	28.57	32.63	65.29
Slope	p	<0.001	<0.001	<0.001	<0.001	0.001	0.001	<0.001
	r	0.95	0.88	0.87	0.84	0.80	0.82	0.90
	SD	4.52	6.74	6.94	7.40	7.29	5.78	3.60
	t	−0.78	−0.39	−0.11	0.32	1.18	2.90	6.76
	p	0.463	0.708	0.917	0.760	0.276	0.023	<0.001
	SD	0.12	0.19	0.21	0.24	0.27	0.25	0.20
	t	11.11	7.28	6.81	6.01	5.34	5.71	8.08
	p	<0.001	<0.001	<0.001	<0.001	0.001	0.001	<0.001

Note. FF$_{IOP}$: fat fraction of IP-OP sequence; FF$_{TEST}$: known fat fraction; SD: standard deviation; F: significance test performed on the linear regression; r: linear goodness of fit; t: paired t test.
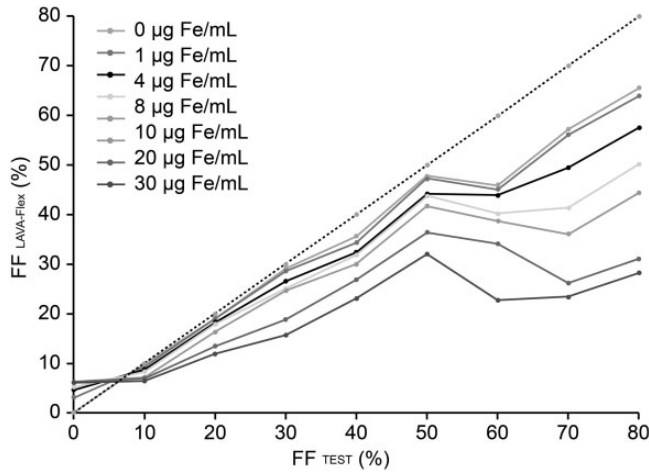*$p < 0.05$; **$p < 0.01$; ***$p < 0.001$.

Figure 4. Changes between the measured and FF$_{TEST}$ components using the LAVA-Flex technique. The FF$_{TEST}$ and FF$_{LAVA-Flex}$ techniques measured the water–oil phantom with iron deposition at concentrations of 0 to 30 µg/mL.

Table 5. Comparison of FF$_{LAVA-Flex}$ (%) and FF$_{TEST}$ (%) by paired t test.

| Iron concentration (µg/mL) | Difference in pairs | | | | t | p |
	Mean	SD	SE	95% CI		
0	5.52	6.36	2.12	0.63–10.41	2.60*	0.031
1	6.22	6.73	2.24	1.04–11.39	2.77*	0.024
4	8.73	8.67	2.89	2.06–15.40	3.02*	0.017
8	11.24	11.70	3.90	2.24–20.24	2.88*	0.020
10	13.41	13.54	4.51	3.00–23.82	2.97*	0.018
20	18.44	17.50	5.83	4.99–31.89	3.16*	0.013
30	21.76	18.83	6.27	7.23–36.24	3.46**	0.008

Note. FF$_{LAVA-Flex}$: fat fraction of LAVA-Flex sequence; FF$_{TEST}$: known fat fraction; SD: standard deviation; SE: standard error; CI: confidence interval.*$p < 0.05$; **$p < 0.01$; ***$p < 0.001$.

Table 6. Linear regression between FF$_{LAVA-Flex}$ (%) and FF$_{TEST}$ (%).

	Test rating	0 µg Fe/mL	1 µg Fe/mL	4 µg Fe/mL	8 µg Fe/mL	10 µg Fe/mL	20 µg Fe/mL	30 µg Fe/mL
Intercept	F	398.92	371.05	306.35	94.83	57.59	22.41	23.82
Slope	p	<0.001	<0.001	<0.001	<0.001	<0.001	0.002	0.002
	r	0.98	0.98	0.98	0.93	0.89	0.76	0.77
	SD	2.49	2.58	2.89	5.21	6.59	9.86	9.75
	t	−1.10	−1.00	−1.24	−0.81	−0.55	−0.09	−0.19
	p	0.307	0.350	0.255	0.445	0.597	0.93	0.856
	SD	0.06	0.07	0.08	0.16	0.22	0.40	0.47
	t	19.97	19.26	17.50	9.74	7.59	4.73	4.88
	p	<0.001	<0.001	<0.001	<0.001	<0.001	0.002	0.002

Note. FF$_{LAVA-Flex}$: fat fraction of LAVA-Flex sequence; FF$_{TEST}$: known fat fraction; SD: standard deviation; F: significance test performed on the linear regression; r: linear goodness of fit; t: paired t test. *$p < 0.05$; **$p < 0.01$; ***$p < 0.001$.
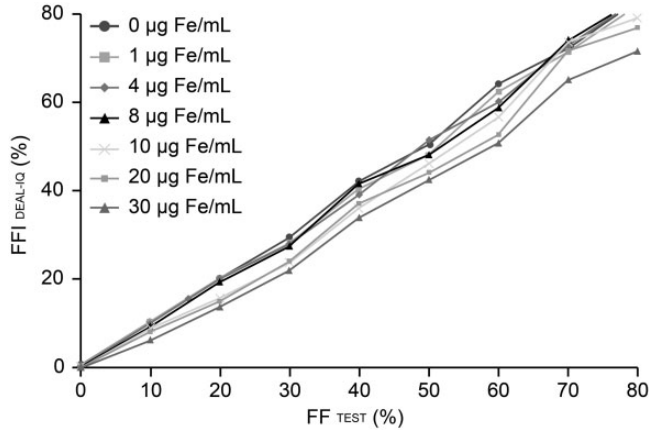
Figure 5. Measurement of FF using the IDEAL IQ technique compared with the FF_{TEST}. The FF_{TEST} and $FF_{IDEAL\ IQ}$ techniques measured the water–oil phantom with iron deposition at concentrations of 0 to 30 µg/mL.

the greater the deviation between the FF_{IOP} and the actual FF_{TEST}. There was a significant difference between the measured FF_{IOP} and FF_{TEST} for iron concentrations ranging from 1 to 30 µg/mL ($p = 0.000$–0.045) and fat components ranging from 10% to 80% ($p = 0.000$–0.038). The 95% CI for the upper limit of the estimated value of the fat content was 40%, meaning that accuracy was low despite the statistically significant linear regression analysis result.

Figure 4 shows the correlation between the $FF_{LAVA-Flex}$ and FF_{TEST} using the LAVA-Flex technique. The statistical analysis results are summarized in Tables 5 and 6. There was a significant difference between the $FF_{LAVA-Flex}$ and FF_{TEST} for iron concentrations from 0 to 30 µg/mL ($p = 0.008$–0.031) and fat components ranging from 10% to 80% ($p = 0.000$–0.027). The 95% CI for the estimated fat content ranged from 0.36% to 36.24%. These findings indicate that even a small amount of iron deposition may result in an error in FF by the IOP and LAVA-Flex techniques based on the two-point Dixon technique. More specifically, FF underestimation

might occur when using the two-point Dixon technique.

Figure 5 shows the correlation between the $FF_{IDEAL\ IQ}$ and FF_{TEST} using the IDEAL IQ technique. The statistical analysis results are summarized in Tables 7 and 8. There was no significant difference between the $FF_{IDEAL\ IQ}$ and FF_{TEST} for iron deposits from 0 to 20 µg/mL. The scatter points of the $FF_{IDEAL\ IQ}$ were very close to those of the FF_{TEST}, and the linear correlation coefficients were high ($r = 0.89$–0.98). The 95% CI for the estimated fat content values by the IDEAL IQ technique was more stable than that of the IOP and LAVA-Flex techniques. Linear correlations between R2* and the known iron concentrations were expectedly high ($r = 0.86$–0.98) as shown in Table 9. As shown in Figure 6, R2* and the iron concentrations were well correlated.

Pathological assessments

Eleven patients were diagnosed with HCC and 15 were diagnosed with liver metastatic tumors from colorectal adenocarcinoma ($n = 6$), pancreatic ductal carcinoma
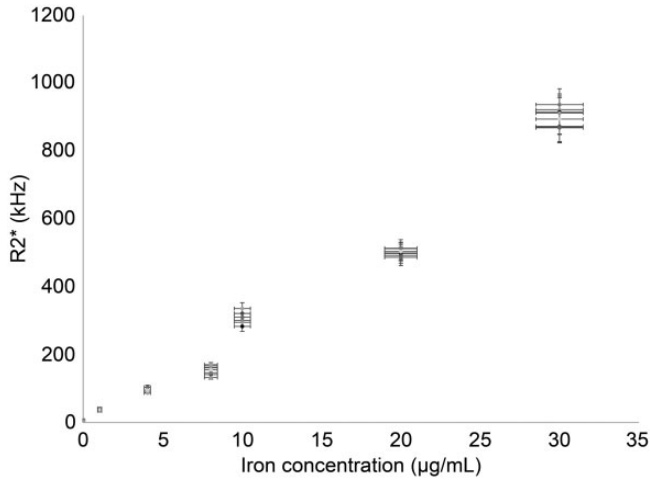
Figure 6. Correlation between iron concentrations and R2* by the IDEAL IQ technique using a water–oil phantom with iron depositions from 0 to 30 μg/mL.

Table 7. Comparison of FF$_{IDEAL\ IQ}$ (%) and FF$_{TEST}$ (%) by paired t test.

Iron concentration (μg/mL)	Difference in pairs				t	p
	Mean	SD	SE	95% CI		
0	−1.48	1.53	0.51	−4.67 to −0.31	−3.913	0.019
1	−0.34	1.56	0.52	−1.54 to 0.85	−0.661	0.527
4	−0.65	1.79	0.59	−2.03 to 0.72	−1.097	0.304
8	−0.33	2.33	0.77	−2.12 to 1.45	−0.429	0.679
10	2.18	2.98	0.99	−0.10 to 4.48	2.203	0.068
20	3.27	3.04	1.01	0.93 to 5.61	2.232	0.071
30	5.88	2.85	0.95	2.31 to 5.78	6.185	0.000

Note. FF$_{IDEAL\ IQ}$: fat fraction of IDEAL IQ sequence; FF$_{TEST}$: known fat fraction; SD: standard deviation; SE: standard error; CI: confidence interval. *$p < 0.05$; **$p < 0.01$; ***$p < 0.001$.

Table 8. Linear regression between FF$_{IDEAL\ IQ}$ (%) and FF$_{TEST}$ (%).

	Test rating	0 μg Fe/mL	1 μg Fe/mL	4 μg Fe/mL	8 μg Fe/mL	10 μg Fe/mL	20 μg Fe/mL	30 μg Fe/mL
Intercept	F	398.92	371.05	306.35	94.83	57.59	22.41	23.82
Slope	p	<0.001	<0.001	<0.001	<0.001	<0.001	0.002	0.002
	r	0.98	0.98	0.98	0.93	0.89	0.96	0.90
	SD	2.49	2.58	2.89	5.21	6.59	9.86	9.75
	t	−1.10	−1.00	−1.24	−0.81	−0.55	−0.09	−0.19
	p	0.307	0.350	0.255	0.445	0.597	0.93	0.856
	SD	0.06	0.07	0.08	0.16	0.22	0.40	0.47
	t	19.97	19.26	17.50	9.74	7.59	4.73	4.88
	p	<0.001	<0.001	<0.001	<0.001	<0.001	0.002	0.002

Note. FF$_{IDEAL\ IQ}$: fat fraction of IDEAL IQ sequence; FF$_{TEST}$: known fat fraction; SD: standard deviation; F: significance test performed on the linear regression; r: linear goodness of fit; t: paired t test. *$p < 0.05$; **$p < 0.01$; ***$p < 0.001$.

Table 9. Linear regression between R2* and iron concentration (µg/mL).

	Test rating	0 µg Fe/mL	1 µg Fe/mL	4 µg Fe/mL	8 µg Fe/mL	10 µg Fe/mL	20 µg Fe/mL	30 µg Fe/mL
Intercept	F	398.92	371.05	306.35	94.83	57.59	52.41	53.82
Slope	p	<0.001	<0.001	<0.001	<0.001	<0.001	0.002	0.002
	r	0.84	0.98	0.98	0.93	0.91	0.86	0.87
	SD	2.49	2.58	2.89	5.21	6.59	9.86	9.75
	t	−1.10	−1.00	−1.24	−0.81	−0.55	−0.09	−0.19
	p	0.307	0.350	0.255	0.445	0.597	0.93	0.856
	SD	0.06	0.07	0.08	0.16	0.22	0.40	0.47
	t	19.97	19.26	17.50	9.74	7.59	4.73	4.88
	p	<0.001	<0.001	<0.001	<0.001	<0.001	0.002	0.002

Note. $R2^*(s^{-1})$: R2* sequence was used to measure the iron quantitation; SD: standard deviation; F: significance test performed on the linear regression; r: linear goodness of fit; t: paired t test. *$p < 0.05$; **$p < 0.01$; ***$p < 0.001$.

(n = 7), and gastric adenocarcinoma (n = 2). The pathological definitions and SAR evaluations for liver steatosis of the liver parenchyma outside the liver lesions were scored, revealing liver steatosis (n = 14), hepatitis (n = 3), and liver fibrosis (n = 9). The SAR in patients without liver cirrhosis (17/26) was 11.31% ± 5.89%, and that in patients with liver cirrhosis (9/26) was 9.84% ± 4.17%.

Patient FF measurements

In the clinical study, the estimated FFs in patients without liver cirrhosis (17/26) were 15.76% ± 6.98%, 16.71% ± 6.77%, and 13.18% ± 6.42% using the IOP, LAVA-Flex, and IDEAL IQ techniques, respectively. The FFs in patients with liver cirrhosis (9/26) were 20.35% ± 6.11%, 20.89% ± 8.49%, and 12.86% ± 4.00%, respectively. The most highly significant correlations were shown between the $FF_{IDEAL\ IQ}$ and the SAR values with or without liver cirrhosis ($r = 0.988$, $p < 0.001$ or $r = 0.970$, $p < 0.001$, respectively).

Discussion

MR imaging is inherently more sensitive to fat and iron deposition than CT and ultrasound.[24–26] MR imaging-based techniques of hepatic fat quantification can identify tiny changes in fat content. This characteristic makes MR imaging an effective tool to quantify hepatic fat and monitor the treatment of hepatic steatosis.[27] However, the signal-based FF is also confounded by many factors, including T1 and T2 bias, T2* decay, the complexity of fat spectral peaks, noise, and J-coupling. Hence, the resulting fat content may be subject to errors in measurement. Iron deposition is an often-encountered complicating factor that may cause local susceptibility changes and alter the T1 and T2 (T2*) relaxation times considerably.[28] Previous studies have shown that up to 40% of patients with NAFLD have iron overload, and growing evidence indicates that lipid accumulation and iron deposition in hepatocytes and Kupffer cells coexist in patients with chronic liver diseases.[29–31]

Recent studies have shown that iron overload has synergistic and promoting effects on the occurrence and development of NAFLD.[19,20] Its mechanism may be associated with hepatocyte fat accumulation, which leads to hypoxia and upregulation of ferritin expression. Upregulation of ferritin expression occurs by reducing the

synthesis of transferrin on the membrane surface, thereby reducing iron output and eventually resulting in accumulation of iron within liver macrophages. Moreover, a preclinical study showed that the hypoxia-inducible factor α concentration increases with exacerbations of non-alcoholic steatohepatitis.[32] Iron overload initiates the Haber–Weiss reaction, generating a large number of oxyradicals that damage hepatocytes and promote cholesterol synthesis, thus accelerating lipid accumulation and liver injury.[20] In a non-alcoholic steatohepatitis mouse model induced by feeding a methionine- and choline-deficent diet, the liver non-heme iron content and serum iron concentration changed significantly at 2 weeks (early stage). Mouse models of hepatic steatosis have further confirmed the synchronization of iron overload and fat accumulation.[33] Overall, evidence has suggested that either qualitative or quantitative assessments of liver fat content must take into consideration the impact of potential iron deposition, which is a challenging but practical issue.

In the present study, a water–oil phantom with iron deposition was constructed, and MR imaging techniques based on signal phase, two-point Dixon, and three-point IDEAL were performed and compared. The Dixon technique achieves decomposition of water and lipids from different proton precession frequencies at known magnetic field strengths to allow calculation of the SI. However, this method is often subject to image phase errors caused by local field inhomogeneity. The spoiled gradient sequence used in IP and OP sequences is sensitive to the choice of flip angle; a flip angle that is too large causes a T1 effect that may lead to a fat quantification error. With higher iron concentrations, the fat content may show large deviations from baseline regardless of the fat content. The observed deviation from the measured fat content ranged from 20.0% to 53.7% in the present study. When the fat content was >50%, a fat saturation phenomenon appeared, and the phantom state had the potential to change from an oil-in-water to a water-in-oil phase. Linear regression shows that when the fat content exceeds 50%, fat prediction begins to stray.

Compared with the IOP technique, the LAVA-Flex image showed better and more homogenous fat suppression and lower magnetic susceptibility artifacts. LAVA-Flex also has the ability to generate water-only and fat-only results using IOP data. However, LAVA-Flex is vulnerable to the presence of iron; with increasing levels of iron deposition, the FF measurements behave similarly to the IOP image. Because of the field inhomogeneity caused by ferritin and hemosiderin that subsequently affect T1, T2, and T2 * relaxations, the reverse in the phase of signal differences may not robustly estimate the water and fat phases. When fat and iron coexist, IOP and LAVA-Flex imaging can both cause difficulty in fat quantification.

The IDEAL IQ technique is a 3D gradient echo imaging method that uses both magnitude and phase information from six echoes that are appropriate for the separation of water and fat signals. Multi-echo acquisition provides robust water and fat separation with T2* correction. T1 bias was largely avoided by using long repetition times and a flip angle of 3°. The spectral complexity of fat as well as noise can be well tolerated using multi-echo complex data. Complex-based techniques can reportedly achieve robust measurements for total fat ranging from 0% to 100%, which overcomes the 50% fat constraint faced by IOP and other two-point Dixon methods.[34] In the present study, the scattering of the FF measurements from the IDEAL IQ was gathered around the straight line of histological fat measurements. The difference between the two FF
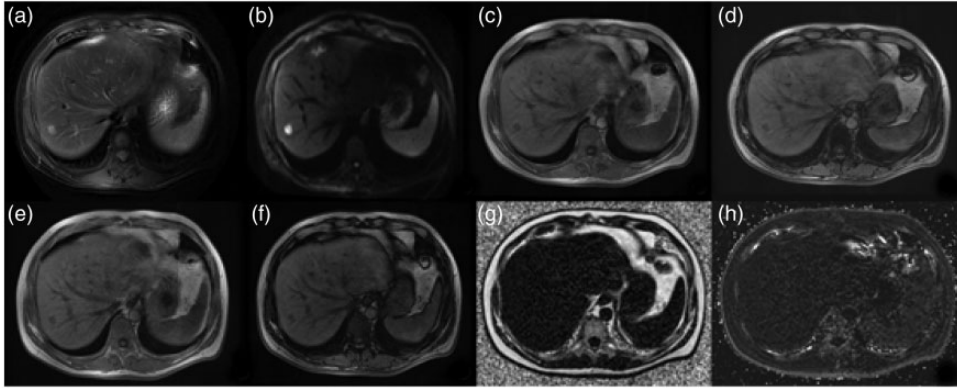
Figure 7. A 53-year-old patient with hepatic metastasis from colorectal primary cancer. He received six courses of neoadjuvant chemotherapy and was in remission from the liver metastasis. (a, b) Hepatic metastases and normal liver tissue outside of the tumor were evaluated for changes in fat content via separate (c, d) water–fat line dual-echo imaging, (e, f) LAVA-Flex imaging, and (g, h) fat mapping and R2* mapping of IDEAL IQ imaging. The three methods achieved measured fat content values of $14.45\% \pm 4.77\%$, $16.39\% \pm 5.85\%$, and $9.61\% \pm 2.13\%$.

measurements was not statistically significant. These technical advantages not only improve the accuracy of fat or iron quantitation but also the reproducibility of the measurements, consistent with a previous study.[35]

R2*estimation of the IDEAL IQ technique is generally performed by fitting an R2* signal model to an acquired multi-echo data set. Noise and fat accumulation in the liver are common challenges in R2* estimation. This study showed that in the presence of a low iron content ($<1\ \mu g/mL$ of iron), the measured R2* was unstable and the measurement variations were too high. This might be related to the magnetic susceptibility artifact around the test tube. R2* and the iron concentration were highly correlated ($R2^* = 0.83–0.98$) regardless of the iron content. The first TE was 1.2 ms, which maintains the signal integrity even with high iron contents. Short echo spacing and first echo time are needed to handle the spectral complexity of the fat signal in case of severe iron overload.

In the clinical study, the FF of the IOP and LAVA-Flex methods overestimated the actual fat content in patients without liver cirrhosis (Figures 7 and 8). The overestimation was more remarkable in patients with liver cirrhosis. These findings indicate that the FF based on the two-Dixon technique can misjudge the fat content because of the disturbance of iron deposition. However, the IDEAL IQ as the modified Dixon technique can be obtained with fly-back gradients for the quantification of hepatic steatosis. Additionally, multiple-site liver FF measurements can be taken for greater precision of the fat content quantification. In the present study, the FF of IDEAL IQ and SAR exhibited excellent correlations without or with liver cirrhosis (Figures 9 and 10). These results indicate that fat content quantification by the IDEAL IQ technique has the ability to be impervious to iron deposition and truly reflects the FF in the liver microenvironment. Together with the advanced fat quantification of the IDEAL IQ sequence, this technique can provide more accurate hepatic fat quantification than other Dixon methods, and the FF of the IDEAL IQ technique can be an optimal choice, especially in patients with
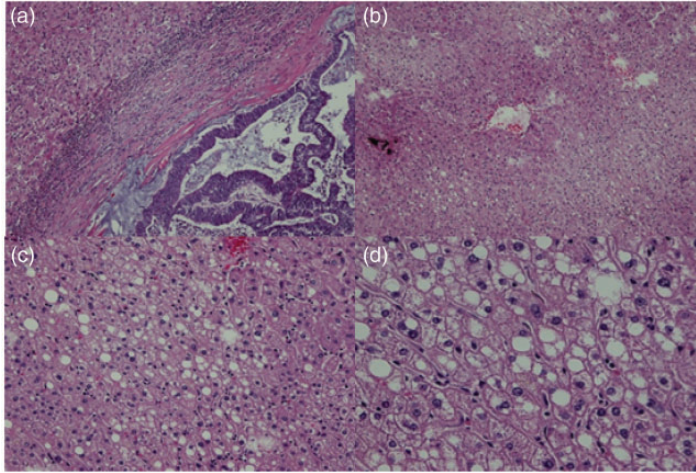
Figure 8. Pathological samples of the focal liver lesions. (a) Liver metastatic tumors from colorectal adenocarcinoma ($\times$5). After a course of neoadjuvant chemotherapy, fat accumulation was observed in normal liver tissue outside of hepatic metastases. (b) Fatty degeneration region in normal liver ($\times$10). (c) Lipid droplet deposition was observed in hepatocytes, and the hepatocytes were markedly altered ($\times$20). (d) Additional image of the hepatocytes with fatty deposition and mild liver steatosis without an inflammatory reaction ($\times$40).
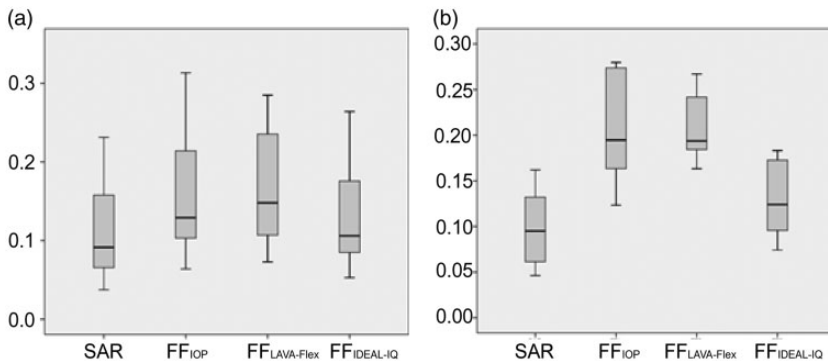

Figure 9. Box plot of SAR distribution. FF_{IOP}, $FF_{LAVA-Flex}$, and $FF_{IDEAL\ IQ}$ in the patients. (a) Patients without liver cirrhosis (17/26). (b) Patients with cirrhosis (9/26).

drug-induced liver injury, repeated transfusion, and chronic diffuse liver diseases and in donor candidates before liver transplantation. Remarkably, there are many parameters related to fat quantification, and the rationality of the parameter setting directly determines the accuracy of fat quantification. Accurate adjustment of relevant parameters must be considered in practical applications. In addition, parameter standardization among different MR imaging devices is necessary to maximize the efficiency of clinical applications of FF quantification.

This study has several limitations. First, the water–oil phantom with iron deposition
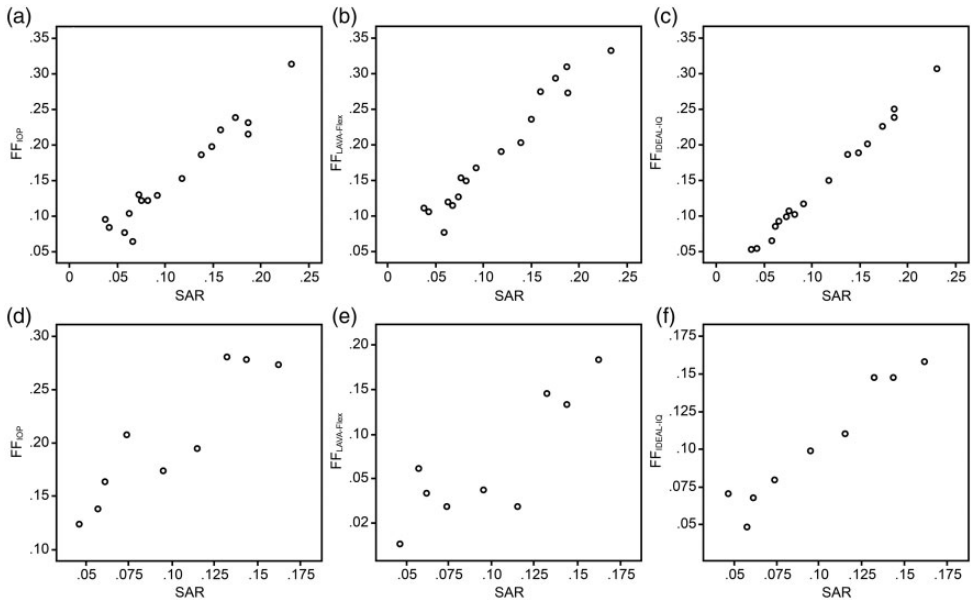
Figure 10. The SAR of the fat content and FF of the three water–fat separation methods in the patients without cirrhosis. (a–c) The SAR of the fat content and FF of the three water–fat separation methods in the patients without cirrhosis; the correlation coefficient was 0.917 to 0.988 ($p < 0.001$). (d–f) The SAR of the fat content and FF of the three water–fat separation methods in the patients with cirrhosis; the correlation coefficient was 0.802 to 0.970 ($p < 0.05$).

cannot completely replace the liver micro-environment *in vivo*. Second, during phantom measurement, the air gap around the test tube generated magnetic susceptibility artifacts, which may have affected the accuracy of the FF and R2* measurements. Third, in the clinical study, the number of patients was small. The number of enrolled patients should be increased in follow-up studies.

Conclusion

The IDEAL IQ technique using complex modeling allows evaluation of at least six peaks in the multi-peak fat spectrum. It can more accurately quantify the FF using the fat-fitting model with iron deposition. In this study, we found that the IDEAL IQ technique can provide a more accurate and robust FF in a complex liver

microenvironment than can the IOP and LAVA-Flex techniques.

Declaration of conflicting interest

The author(s) declare that there is no conflict of interest.

ORCID iD

Li Yang (iD) http://orcid.org/0000-0002-7432-8178

References

1. Willebrords J, Pereira IV, Maes M, et al. Strategies, models and biomarkers in experimental nonalcoholic fatty liver disease research. *Prog Lipid Res* 2015; 59: 106–125. doi: 10.1016/j.plipres.2015.05.002.

2. Clark JM and Diehl AM. Nonalcoholic fatty liver disease: an under recognized cause of cryptogenic cirrhosis. *JAMA* 2003; 289: 3000–3004. doi: 10.1001/jama.289.22.3000.

3. Milic S and Stimac D. Nonalcoholic fatty liver disease/steatohepatitis: epidemiology, pathogenesis, clinical presentation and treatment. *Dig Dis* 2012; 30: 158–162. doi: 10.1159/000336669.

4. Yilmaz Y. NAFLD in the absence of metabolic syndrome: different epidemiology, pathogenetic mechanisms, risk factors for disease progression. *Semin Liver Dis* 2012; 32: 14–21. doi: 10.1055/s-0032-1306422.

5. Sharma A, Houshyar R, Bhosale P, et al. Chemotherapy induced liver abnormalities: an imaging perspective. *Clin Mol Hepatol* 2014; 20: 317–324. doi: 10.3350/cmh.2014.20.3.317.

6. Robinson SM, Wilson CH, Burt AD, et al. Chemotherapy-associated liver injury in patients with colorectal liver metastases: a systematic review and meta-analysis. *Ann Surg Oncol* 2012; 19: 4287–4299. doi: 10.1245/s10434-012-2438-8.

7. Gomez Dorronsoro ML, Vera R, Ortega L, et al. Recommendations of a group of experts for the pathological assessment of tumour regression of liver metastases of colorectal cancer and damage of non-tumour liver tissue after neoadjuvant therapy. *Clin Transl Oncol* 2014; 16: 234–242. doi: 10.1007/s12094-013-1104-3.

8. Chalasani NP, Hayashi PH, Bonkovsky HL, et al. Clinical Guideline: the diagnosis and management of idiosyncratic drug-induced liver injury. *Am J Gastroenterol* 2014; 109: 950–966. doi: 10.1038/ajg.2014.131.

9. Bjornsson ES. Epidemiology and risk factors for idiosyncratic drug-induced liver injury. *Semin Liver Dis* 2014; 34: 115–122. doi: 10.1055/s-0034-1375953.

10. Busuttil RW and Tanaka K. The utility of marginal donors in liver transplantation. *Liver Transpl* 2003; 9: 651–663. doi: 10.1053/jlts.2003.50105.

11. Mito S, Ishizaka K, Nakanishi M, et al. Comparison of fat suppression techniques of bilateral breast dynamic sequence at 3.0T: utility of three-point DIXON technique. *Nihon Hoshasen Gijutsu Gakkai Zasshi* 2011; 67: 654–660.

12. Ishizaka K, Oyama N, Mito S, et al. Comparison of 1H MR spectroscopy, 3-point DIXON, and multi-echo gradient echo for measuring hepatic fat fraction. *Magn Reson Med Sci* 2011; 10: 4–8.

13. Keese D, Korkusuz H, Huebner F, et al. In vivo and ex vivo measurements: noninvasive assessment of alcoholic fatty liver using 1H-MR spectroscopy. *Diagn Interv Radiol* 2016; 22: 13–21. doi: 10.5152/dir.2015.14331.

14. Peng X, Ju S, Qin Y, et al. Quantification of liver fat in mice: comparing dual-echo Dixon imaging, chemical shift imaging, and 1H-MR spectroscopy. *J Lipid Res* 2011; 52: 1847–1855. doi: 10.1194/jlr.D016691.

15. Dong Z, Luo Y, Zhang Z, et al. MR quantification of total liver fat in patients with impaired glucose tolerance and healthy subjects. *PloS One* 2014; 9: e111283. doi: 10.1371/journal.pone.0111283.

16. Chebrolu VV, Hines CDG, Yu H, et al. Independent estimation of T2* for water and fat for improved accuracy of fat quantification. *Magn Reson Med* 2010; 63: 849–857. doi: 10.1002/mrm.22300.

17. Hines CD, Yu H, Shimakawa A, et al. T1 Independent, T2* corrected MRI with accurate spectral modeling for quantification of fat: validation in a fat-water-SPIO phantom. *J Magn Reson Imaging* 2009; 30: 1215–1222. doi: 10.1002/jmri.21957.

18. Amdrews M and Arredondo M. Hepatic and adipocyte cells respond differentially to iron overload, hypoxic and inflammatory challenge. *Biometals* 2012; 25: 749–759. doi: 10.1007/s10534-012-9543-9.

19. Valenti L, Fracanzani AL, Bugianesi E, et al. HFE genotype, parenchymal iron accumulation, and liver fibrosis in patients with nonalcoholic fatty liver disease. *Gastroenterology* 2010; 138: 905–912. doi: 10.1053/j.gastro.2009.11.013.

20. Granham RM, Chua AC, Carter KW, et al. Hepatic iron loading in mice increases cholesterol biosynthesis. *Hepatology* 2010; 52: 462–471. doi: 10.1002/hep.23712.

21. Hernando D, Cook RJ, Diamond C, et al. Magnetic susceptibility as a B0 field strength independent MRI biomarker of liver iron overload. *Magn Reson Med* 2013; 70: 648–656. doi: 10.1002/mrm.24848.

22. Hernando D, Liang ZP and Kellman P. Chemical shift-based water/fat separation: a comparison of signal models. *Magn Reson Med* 2010; 64: 811–822. doi: 10.1002/mrm.22455.

23. Chai X, Li D, Cao X, et al. ROS-mediated iron overload injures the hematopoiesis of bone marrow by damaging hematopoietic stem/progenitor cells in mice. *Sci Rep* 2015; 5: 10181. doi: 10.1038/srep10181.

24. Reeder SB, Cruite I, Hamilton G, et al. Quantitative assessment of liver fat with magnetic resonance imaging and spectroscopy. *J Magn Reson Imaging* 2011; 34: 1–37. doi: 10.1002/jmri.22775.

25. Hernando D, Levin YS, Sirlin CB, et al. Quantification of liver iron with MRI: state of the art and remaining challenges. *J Magn Reson Imaging* 2014; 40: 1003–1021. doi: 10.1002/jmri.24584.

26. Sharma P, Altback M, Galons JP, et al. Measurement of liver fat fraction and iron with MRI and MR spectroscopy techniques. *Diagn Interv Radiol* 2014; 20: 17–26. doi: 10.5152/dir.2013.13124.

27. Noureddin M, Lam J, Peterson MR, et al. Utility of magnetic resonance imaging versus histology for quantifying changes in liver fat in nonalcoholic fatty liver disease trials. *Hepatology* 2013; 58: 1930–1940. doi: 10.1002/hep.26455.

28. Kuhn JP, Hernando D, Munoz del Rio A, et al. Effect of multipeak spectral modeling of fat for liver iron and fat quantification: correlation of biopsy with MR imaging results. *Radiology* 2012; 265: 133–142. doi: 10.1148/radiol.12112520

29. George DK, Goldwurm S, MacDonald GA, et al. Increased hepatic iron concentration in nonalcoholic steatohepatitis is associated with increased fibrosis. *Gastroenterology* 1998; 114: 311–318.

30. Moirand R, Mortaji AM, Loreal O, et al. A new syndrome of liver iron overload with normal transferrin saturation. *Lancet* 1997; 349: 95–97. doi: 10.1016/S0140-6736(96)06034-5

31. Queiroz-Andrade M, Blasbalg R, Ortega CD, et al. MR imaging findings of iron overload. *Radiographics* 2009; 29: 1575–1589. doi: 10.1148/rg.296095511.

32. Csak T, Bala S, Lippai D, et al. MicroRNA-122 regulaters hypoxia-inducible factor-1 and vimentin in hepatocytes and correlates with fibrosis in diet-induced steatohepatitis. *Liver Int* 2015; 35: 532–541. doi: 10.1111/liv.12633.

33. Xin HG, Zhang BB, Wu ZQ, et al. Treatment with baicalein attenuates methionine-choline deficient diet induced nonalcoholic steatohepatitis in rats. *Eur J Pharmacol* 2014; 738: 310–318. doi: 10.1016/j.ejphar.2014.06.006.

34. Bornert P, Keupp J, Eggers H, et al. Whole-body 3D water/fat resolved continuously moving table imaging. *J Magn Reson Imaging* 2007; 25: 660–665. doi: 10.1002/jmri.20861.

35. Cher HT and Sudhakar KV. Magnetic resonance elastography and other magnetic resonance imaging techniques in chronic liver disease: current status and future direction. *Gut Liver* 2016; 10: 672–686. doi: 10.5009/gnl15492.